Solar Energy Materials & Solar Cells 290 (2025) 113697

Contents lists available at ScienceDirect

Solar Energy Materials and Solar Cells

journal homepage: www.elsevier.com/locate/solmat

Low-cost carbazole and phenothiazine based trimer molecules as hole transporting materials for inverted perovskite solar cells

Valentina Maruzzo [a,b], Antoine Bousquet [a], Fabio Matteocci [c], Elisa Nonni [c], Daimiota Takhellambam [c], Raffaele Borrelli [e], Damiano Mangatia [e], Eric Grelet [f], Mamatimin Abbas [g], Mathieu G. Silly [h], Matteo Bonomo [b,j], Aldo Di Carlo [c], Claudia Barolo [b,d,i], Nadia Barbero [b,d], Christine Lartigau-Dagron [a,*]

[a] Universite de Pau et Pays de l'Adour, CNRS, IPREM, Pau, France
[b] Department of Chemistry, NIS Interdepartmental and INSTM Reference Centre, University of Torino, Italy
[c] C.H.O.S.E. (Centre for Hybrid and Organic Solar Energy), Department of Electronic Engineering, University of Rome-Tor Vergata, Italy
[d] Institute of Science, Technology and Sustainability for the Development of Ceramic Materials (ISSMC-CNR), Faenza, Italy
[e] Department of Agricultural, Forest and Food Sciences, University of Turin, Italy
[f] Univ. Bordeaux, CNRS, CRPP, UMR 5031, F-33600, Pessac, France
[g] IMS, University of Bordeaux, CNRS, UMR-5218, Bordeaux INP, ENSCBP, 33405, Talence, France
[h] Synchrotron SOLEIL, L'Orme des Merisiers, Départementale 128, 91190, Saint-Aubin, France
[i] ICxT Interdepartmental Centre, University of Torino, Italy
[j] Department of Basic and Applied Sciences for Engineering (SBAI), La Sapienza University of Rome, Via Del Castro Laurenziano 7, 00161, Roma, Italy

A B S T R A C T

Phenothiazine (P) and Carbazole (C) are low-cost scaffolds widely used in the synthesis of Hole Transporting Materials (HTMs) for Perovskite Solar Cells (PSCs). So far, these compounds have been assembled together forming HTMs applied exclusively in direct cell architectures with the necessity of dopants to improve power conversion efficiencies (PCEs). In this work, two trimer molecules with opposite structure, namely CPC and PCP, have been designed, synthesized and implemented without any dopant in inverted PSCs. We assessed the impact of the molecular design on the final device performances, in view of the different intrinsic features. Both HTMs optoelectronic properties have been investigated along with a computational study by DFT. For optimizing the implementation in PSCs, thermal annealings and decrease of HTM concentration have been considered. PCP outperformed CPC, with an average PCE of 14.1 % against 10.4 %, achieving comparable performances to PTAA reference device (14.5 %). No hysteresis was observed for all devices and high FF reaching almost 80 % were obtained with PCP-based devices. The performances of the HTMs were correlated with the electronic behaviour observed by synchrotron-based soft X-ray photoelectron spectroscopy (PES). Secondary electron cut-off analysis highlighted a favourable work-function modification and the presence of high intermolecular interaction along with better energetic alignment for PCP, which contributed to its enhanced performances. Complementary characterizations by transient photocurrent and transient photovoltage confirmed the positive effect of decreasing the HTM concentration as observed in devices. Steady state and time resolved photoluminescence experiments corroborated the improved charge carrier dynamics and recombination features for PCP.

1. Introduction

The growth of the world population and its energy demand increase the importance of renewable resources development. Solar energy is one of the most abundant among these resources, and intense research efforts have been devoted to improving the performances, scalability and stability of photovoltaic devices. Among the emerging photovoltaic technologies, perovskite solar cells (PSCs) received great attention from the research community due to the rapid increase of power conversion efficiency (PCE), which reached 26.2 % for a n-i-p single junction (lab scale certified device) [1–3]. However, the traditional n-i-p architecture has shown problems of stability and hysteresis [4]. Indeed, the dopants typically used to enhance the conductivity of the hole transporting layer (HTL) decrease the device long-term stability, as they tend to absorb moisture, responsible for accelerating the perovskite degradation or causing Li^+ migration in the perovskite layer [5,6]. Additionally, the high temperatures required for the sintering of the metal oxide electron transporting material (ETM) can represent a problem when heat sensitive materials or flexible devices are employed.

In the inverted p-i-n architecture, the HTL is deposited directly on the

* Corresponding author.
E-mail address: christine.lartigau-dagron@univ-pau.fr (C. Lartigau-Dagron).

https://doi.org/10.1016/j.solmat.2025.113697
Received 12 March 2025; Received in revised form 2 May 2025; Accepted 7 May 2025
Available online 22 May 2025

substrate, followed by the perovskite, the ETM and the top electrode deposition. In this configuration the hysteresis is significantly reduced and the stability is higher [4]. In most cases, the charge transport layers do not require the addition of dopants, and the fabrication costs are lower as metals like Al and Cu can be used as back electrodes instead of Au required in the n-i-p architecture [7]. However, their power conversion efficiency (PCE) lags behind their regular counterpart, and rarely exceeds 23 %, due to several recombination pathways [8]. In fact, the quality of the perovskite layer is strongly affected by the HTL on which it grows [7]. Thus, in addition to the usual requirements [9], suitable surface properties of the HTL are essential to ensure the correct crystallization of a perovskite film with low defect density. Poly[bis (4-phenyl) (2,4,6-trimethylphenyl) amine] (PTAA) represents one of the most used and efficient hole transporting material (HTM) in inverted PSCs, thanks to its relatively simple fabrication process and its good stability. However, the low batch-to-batch reproducibility, the high synthetic cost [6], alongside the unmatched energy levels, are not negligible drawbacks. Furthermore, additional post-treatments of the surfaces and interlayers are often necessary to reduce the defects at the buried interfaces [10]. Another promising category of HTLs are the self-assembled monolayers (SAMs), in which we can find carbazole core molecules like [2-(9H-Carbazol-9-yl) ethyl]phosphonic Acid (2-PACz) or [2-(3,6-dimethoxy-9*H*-carbazol-9-yl) ethyl]phosphonic acid (MeO-2-PACz). These molecules offer low production costs, easily tuneable energy levels and surface properties, and extremely low electronic losses once incorporated into the devices. However, they can suffer from limited thermal and light stability, depending on the anchoring group [11].

Given the limitations of reference HTMs present in the literature, here is ongoing demand for efficient, stable and cost-effective HTMs. Phenothiazine and carbazole scaffolds present a low cost (lower to 1 €. g^{-1} in the case of carbazole and 0.1 €.g^{-1} for phenothiazine) and favourable and easily tuneable electronic properties. Phenothiazine displays a butterfly shape and can form a stable radical cation with reversible oxidation and low potential [12], whereas carbazole is a planar heterocyclic scaffold exhibiting advantageous processing properties that allow for an effective hole extraction and transport [13]. They have been widely used as main HTM scaffolds of the PSCs [14–17], with studies probing the effect of their presence on the solar cell performances by using the same central or peripheral scaffold, bearing either a phenothiazine or a carbazole unit [18–20]. Furthermore, they have been assembled together to create new HTMs: a carbazole central core was linked to the nitrogen of phenothiazine units at its 3,6 positions by Lengvinaite et al. [21] in 2007 or at the nitrogen atom by Li et al. [22] in 2018. A phenothiazine central core was linked at the 3,7 positions to the nitrogen of carbazole peripheral units by Huang et al. [23] in 2021. Trimers consisting of an alternation of phenothiazine and carbazole spaced by a double bond or directly linked were synthesized by Zhang et al. [24] in 2018 and Wang et al. [25] in 2022, respectively. In all cases, the molecules were implemented in n-i-p architectures in the presence of LiTFSI and tBP as dopants, whose detrimental activity towards the final device stability is well known from literature [5,9, 26–28], reaching PCEs ranging from 14 up to 16.5 %. P- and C- containing derivatives have thus never been implemented in p-i-n devices in the absence of any dopants to the best of our knowledge.

Herein, we designed and synthesized two trimers based on phenothiazine and carbazole units, 10-hexyl-3,7-bis(9-hexyl-9H-carbazol-3-yl)-10H-phenothiazine and 3,3'-(9-hexyl-9H-carbazole-3,6-diyl)bis (10-hexyl-10H-phenothiazine), referred as CPC and PCP respectively, that are presented in Scheme 1. The optoelectronic properties of the molecules were assessed by UV–visible absorption, photoluminescence and cyclic voltammetry. The molecules showed an absorption in the UV region, an emission from 400 to 500 nm (in the absorption range of the perovskite), and a HOMO level compatible with the valence band of the active layer. A computational study based on density functional theory (DFT) was performed to give more insights into the nature of the electronic transitions. Both molecules were implemented in p-i-n PSCs using the high bandgap double cation perovskite $Cs_{0.17}FA_{0.83}Pb(I_{0.80}Br_{0.20})_3$ [29], which is well suited for a further tandem application. The performances of the two newly developed HTMs were investigated considering different conditions of thermal annealing and HTM concentration and compared to the PTAA reference. Synchrotron-based photoelectron spectroscopy (PES) analyses enable to explain the different performances obtained: remarkable differences in the electronic behaviour and the work-function modifications were revealed by the Secondary electron cut-off photoemission spectra analysis. To get more insights in the charge carrier dynamics and recombination pathways for both molecules, transient photocurrent, transient photovoltage (to also investigate the effect of HTM concentration decrease), as well as steady state and time resolved photoluminescence experiments were performed.

2. Materials and methods

2.1. Materials

Materials and Instruments: Unless otherwise stated, all the chemicals and solvents were purchased from Sigma-Aldrich, VWR, Carlo Erba, Merck, Fluka, Alfa Aesar and TCI and used as received. NMR solvents were purchased from Sigma-Aldrich and Euriso-top. All reactions were monitored with analytical TLC (Merck Kieselgel 60 F254). Column chromatography was carried out with Biotage Isolera and Buchi Pure C-850 FlashPrep with silica gel particle size 60 μm. PTAA was purchased from Solarischem (Mw of 15 KDa, pdi 1.3). Glass/ITO substrates (10 Ω

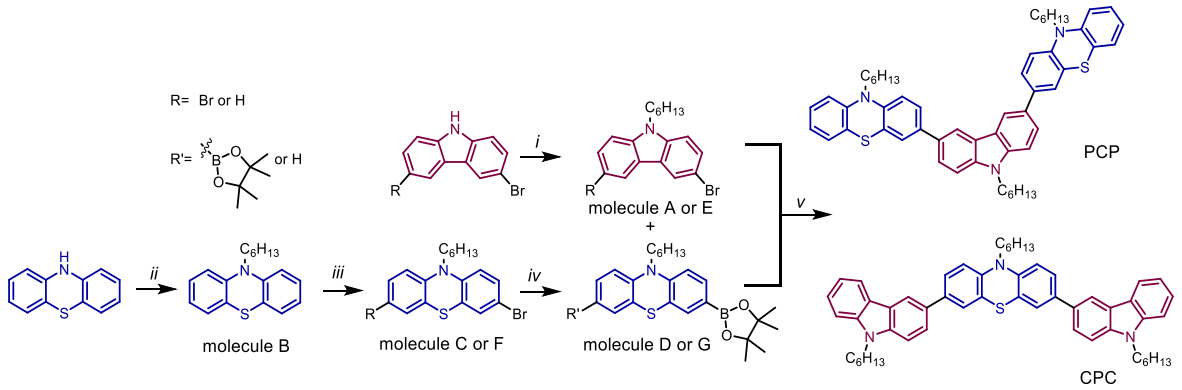

Scheme 1. Synthetic strategy of PCP and CPC compounds. i) 1) KOH, THF, 50 °C, 1 h; 2) Br-hexane, reflux, 3 h. ii) 1) NaH, DMF, 0 °C, 1 h; 2) I-hexane, room temperature, overnight. iii) if mono-bromination: NBS, DMF, room temperature, overnight; if di-bromination: Br_2, CH_3COOH, room temperature, one day. iv) B_2Pin_2, $Pd(PPh_3)_2Cl_2$, KOAc, toluene, reflux, overnight. v) $Pd(PPh_3)_4$, Aliquat 336, toluene and water, 110 °C, 48 h.

sq−1) were purchased from Kintec.

2.2. Synthesis

2.2.1. 3,3'-(9-hexyl-9H-carbazole-3,6-diyl)bis (10-hexyl-10H-phenothiazine), PCP

The different synthetic steps for the preparation of the functionalized scaffolds (see Scheme 1) are presented in supplementary information. 3,6-dibromo-9-hexyl-9H-carbazole (0.235 g, 0.57 mmol) was placed in a reaction tube along with 10-hexyl-3-(4,4,5,5-tetramethyl-1,3,2-dioxaborolan-2-yl)-10H-phenothiazine (0.47 g, 2 eq.), the catalyst Tetrakis (triphenylphosphine) palladium (33 mg, 0.05 eq.), aliquat®336 (0.101 g, 0.2 eq.) and 2.85 ml of toluene. Potassium carbonate K_2CO_3 (0.396 g, 5 eq.) was dissolved in 0.63 ml of water (previously degassed), and the resulting solution was added to the reaction mixture, which was sealed, further degassed and heated at 100 °C for two days. Once the reaction was completed, the organic phase was separated from the water, which was further extracted with dichloromethane DCM (3 × 8 ml). The joined organic phases were reduced in volume and passed through a short pad of Celite before drying with Na_2SO_4 and remotion of the solvent. The crude product was solubilised in DCM again precipitated in methanol MeOH (volume 60 times that of DCM). The solid was isolated by centrifugation, rinsed with MeOH. 258 mg of pure product (55 % yield) as a yellow powder were obtained. [M+] exact mass = 813.42, MS (ESI-MS) = 813.2, see supplementary information for NMR characterizations.

2.2.2. 10-Hexyl-3,7-bis(9-hexyl-9H-carbazol-3-yl)-10H-phenothiazine, CPC

The general procedure used is similar to that of PCP presented above, considering 10-hexyl-3,7-bis(4,4,5,5-tetramethyl-1,3,2-dioxaborolan-2-yl)-10H-phenothiazine (0.51 g, 0.95 mmol) placed in a reaction tube with 3-bromo-9-hexyl-9H-carbazole (0.676 g, 2.15 eq.) and the palladium catalyst (55 mg, 0.05 eq.), aliquat®336 (0.168 g, 0.2 eq.) and 4.75 ml of toluene. The crude product was purified by multiple precipitation from DCM in MeOH to get 343 mg of pure product (46 % yield) as a yellow powder. [M+] exact mass = 781.44, MS (ESI-MS) = 780.8, see supplementary information for NMR characterizations.

2.3. Characterizations

^{1}H NMR (600 MHz) and ^{13}C NMR (151 MHz) spectra were recorded at 25 °C on a Bruker Avance 600 NMR and are reported as chemical shifts (δ) in ppm relative to TMS(δ = 0). Mass spectra (ESI-MS) were obtained on a Varian 325-MS TQ Mass Spectrometer. Absorption spectra were measured on a Shimadzu UV-1900i UV–Vis Spectrophotometer, using a resolution of 0.5 nm. Steady state emission spectra were measured on a Shimadzu RF-6000 with excitation at the maximum absorption wavelength, and resolution at 0.5 nm. Electrochemical characterization (CV) was performed by means of a SP-300 BIOLOGIC potentiostat. A three-electrode set-up was employed with an Au or carbon black as the working electrode, a Pt wire as the counter-electrode and Ag/AgCl as the reference electrode. For the analysis of the molecules a solution of them in DCM containing tetrabutylammonium hexafluorophosphate ($TBAPF_6$, 0.1 M) as the supporting electrolyte was done. CVs were recorded at 50 mV s^{-1}. Ferrocene was used as internal standard. Thermogravimetric analyses (TGA) were performed on a Q600 SDT TA instrument under N_2 from 30 to 900 °C with a ramp of 10 °C. min^{-1}, while Differential Scanning Calorimetry (DSC) analyses were performed under N_2 as well, from 30 °C to 300 °C, with a ramp of 10 °C. min^{-1} on a DSC 3 star Matter Toledo. Wide angle X-ray scattering experiments were carried out on a XEUSS 2.0 device (XENOCS, France) working at a wavelength of 1.54 Å (Cu K_α emission) and with a sample-to-detector distance of 347.8 mm calibrated with Silver Behenate standard. Typical exposure time was 1 h, and the scattered signal was collected on a two-dimensional PILATUS-300 k detector (DECTRIS, Switzerland) located perpendicularly to the direct beam. PCP and CPC samples were loaded in quartz capillaries (WJM-Glas/Müller GmbH, Germany) of 1.5 mm in diameter, and placed into a heating stage having a thermal stability of 0.1 °C. PES and NEXAFS experiments were performed on the TEMPO beamline at the synchrotron SOLEIL in France [30]. The beamline is equipped with two insertion device (HU80 and HU44 Apple II undulators) set to deliver linear horizontal biased soft X-ray photons. The energy range covered by the beamline goes from 50 to 1500 eV. The resolving power of the beamline is higher than 10 000. PES measurements are done at normal emission from the sample. The photoelectrons are collected by a high-resolution MBS A-1 photoelectron analyzer equipped with a delay line detector developed by Elettra [31]. The base pressure of the analysis chamber is lower than 5.10^{-10} mbar. PES analyses were carried out on the ITO substrates (previously subjected to UV-O_3 treatment) on which the two molecules were deposited by spin coating (4000 r.p.m. for 30 s with a dynamic deposition) from a solution of 2 mg ml^{-1} in THF. The precise excitation photon energy is determined by measuring the first and second orders of the Au4f core level spectra and the corresponding Fermi level position of a referenced clean gold substrate. PES spectra are plotted relative to the Fermi level energy position measured on a referenced clean gold substrate for the different photon energies used. NEXAFS spectra are measured in total electron yield (sample current) at the C K edge for different beam incident angle. The transmission of the beamline is measured with a gold mesh. The NEXAFS spectra are corrected from the transmission of the beamline and normalized to the background. The hole transport properties were investigated through the preparation of organic field-effect transistors (OFETs) with the following composition $n^{++}Si/SiO_2$ (100 nm)/poly (1-vinyl-1,2,4-triazole) (10 nm)/HTM/MoO_3 (10 nm)/Ag (50 nm). Transfer curves were recorded. Although the drain currents were relatively low, gate currents were monitored to be not scaling with the drain current. Mobility values were derived by linearly fitting the square root of the drain current and taking into account the geometric parameters (L = 50 μm, W = 1 mm) of the transistors.

Device characterizations: The current density-voltage (J-V) curves were measured in air atmosphere by using a solar simulator (ABET Sun 2000, class A) at AM1.5 and 100 mW cm^{-2} illumination conditions, calibrated with a certified reference Si Cell (RERA Solutions RR-1002). Masks of 0.09 cm^2 were used to perform the measurement. Incident power was measured with a Skye SKS 1110 sensor. Both reverse and forward J–V scans were performed by using a scan rate of 50 mV s^{-1}. Photovoltaic parameters are given as average values on at least 12 devices. IPCE measurements were performed through a commercial apparatus (Arkeo all-in-one measurement platform) provided by Cicci Research. The albedo radiation was provided by 2 different white LEDs from Osram (4000 K) for the irradiance ranges 0–3 mW cm^{-2} and 3–22 mW cm^{-2} respectively. TPV and TPC were measured with a commercial apparatus (Arkeo, Cicci Research s. r.l.) based on a high-speed Waveform Generator that drives a high-speed LED (5000 K). The device is connected to a transimpedance amplifier and a differential voltage amplifier to monitor short circuit current or open circuit voltage. The parameters used for TPC and TPV characterization were: Duty Cycle = 0.3, Sampling Time: 10 ns, Time Duration: 200 μs. Steady-State and Time-resolved PL (TRPL) were collected by using a modular testing platform (Arkeo-Cicci Research s. r.l.).

2.4. Computational study

The computational study was performed based on density functional theory (DFT) methodologies, using the ωB97X-D functional [32] with the def2-TZVP Ahlrich's basis set. Solvent effects have been included using the CPCM implementation. All calculations have been performed using the ORCA software [33].

2.5. Device fabrication

A glass/ITO sheet of a thickness of 1.1 mm was laser etched, labelled

and cut to square of 2.5*2.5 cm^2. The substrates were washed with a solution of 1 % of Hellmanex in water and sonicated for 10 min. Subsequently, the substrates were rinsed with water and sonicated with acetone and isopropanol (IPA) for 10 min each. Finally, UV-O_3 treatment was performed for 15 min before their use in a nitrogen filled glovebox. The HTM solutions were prepared in a nitrogen filled glovebox using anhydrous solvents: 2 mg of PTAA in 1 ml of toluene, PCP and CPC molecules prepared as solution in tetrahydrofuran (THF) at different concentrations. The solutions were left under stirring overnight and filtered with a 0.45 μm PTFE filter the day after, before the deposition. The perovskite solution was prepared the day before, left stirring overnight to allow a complete dissolution of the salts, at a concentration of 1.2M. Each precursor salt (PbI_2 0.8724 mmol ml^{-1}, $PbBr_2$ 0.3653 mmol ml^{-1}, CsI 0.2038 mmol ml^{-1} and FAI 0.9962 mmol ml^{-1}) was weighed individually and dissolved in a mixture of anhydrous DMSO: DMF (1:4). The ETMs solution were prepared dissolving 27 mg of $PC_{61}BM$ in 1 ml of a solution of chlorobenzene:dichlorobenzene (CB: DCB - 3:1). The solution was left 1 h at 70 °C before filtering it. The BCP solution was prepared weighting 0.5 mg in 1 ml of IPA. The device fabrication was carried out in glovebox. PTAA cells: 80 μl of the solution were statically spin coated at 5000 r.p.m. for 20 s with an acceleration time of 2 s. To these cells, an annealing at 100 °C for 10 min was done. PCP and CPC cells: 90 μl of the solution were dynamically spin coated at 4000 r.p.m. for 30 s with an acceleration time of 2 s. The annealing procedure was applied. When the substrates cooled down to room temperature, 100 μl of perovskite solution was statically spin coated at 5000 r.p.m. for 35 s with an acceleration time of 5 s. Prior to 15s before end, 150 μl of the antisolvent CB were dropped followed by annealing at 100 °C for 15 min. Then, 100 μl of $PC_{61}BM$ solution was statically spin coated at 1800 r.p.m. for 20 s with an acceleration time of 2 s, followed by an annealing at 100 °C for 3 min. Finally, the BCP solution was spin coated at 4000 r.p.m. for 15 s with an acceleration time of 2 s. The copper electrode was evaporated with a final thickness of 100 nm at 0.1–1.0 $Å s^{-1}$ rate. The active area of the final PSC was 0.16 cm^2.

3. Results and discussion

3.1. Synthesis and structural characterization

Phenothiazine and carbazole were selected as main scaffolds to synthesize PCP and CPC, two molecule HTMs having reverse backbones (Scheme 1).

Both mono-brominated or di-brominated carbazoles were alkylated following literature protocols [34,35] and purified through either a short pad of silica (in the case of the mono-brominated derivative) or through crystallization (in the case of the di-brominated derivative) [36]. They were obtained in high yields (>90 %, see supplementary information).

The phenothiazine substrate was first alkylated following a synthetic protocol previously developed by our group [37] and then purified by column chromatography to obtain the pure product [38], on which the bromination reaction was performed. The di-brominated derivative was easily synthesized following the literature protocols [39] and purified by precipitation once increased its purity degree with a quick column chromatography. By contrast, the mono-brominated derivative was more difficult to synthesize despite numerous protocols present in the literature [40,41]. Different reaction conditions were tested and the desired product was obtained with a yield of 45.5 % and a purity of 95 % upon optimization of reaction conditions. The brominated derivatives were converted into the corresponding boronic esters with a Miyaura borylation reaction [39,41,42]. Finally, the brominated and borylated scaffolds underwent a Suzuki reaction in heterogeneous environment to obtain the two molecules, using protocols optimized from literature [39,43]. The attempt of a purification by chromatography caused remarkable losses in the yield, probably due to the formation of π-π stacked aggregates, not able to be eluted once adsorbed onto silica, even using elution phases with high polarity. Thus, precipitation was chosen to purify the products, leading to the pure product with a yield of 55 % and 46 % for PCP and CPC, respectively. The HTMs were structurally characterized by ^1H NMR, ^{13}C NMR, 2D-NMR H-H COSY technique and high-resolution mass spectrometry. The detailed characterizations are consistent with the expected structures and can be found in the supporting information.

3.2. Optical and electrochemical properties of the HTMs

Once the purity of the obtained molecules was ensured, their optical, electrochemical and thermal properties have been investigated.

A combination of UV–VIS absorption and fluorescence spectroscopies was performed both on THF solutions and films (Fig. 1). When solubilised in THF, PCP displayed a maximum absorbance wavelength at 263 nm, with a shoulder at 300 nm and a molar extinction coefficient (ε) at λ_{max} of 82 000 M^{-1} cm^{-1}. CPC showed a maximum absorbance at 289.5 nm, a shoulder at 340 nm and a ε at λ_{max} of 82 900 M^{-1} cm^{-1} (Fig. 1a). The two bands in the range of 250–300 nm and 300–350 nm were attributed by literature to the π-π* transition of the carbazole scaffolds [25], and were investigated through DFT studies (paragraph 3.3). Since the materials are implemented as HTLs in the solar cells, their optical properties in film have also been characterized. A solution of 15 mg ml^{-1} in THF of both molecules was spin coated on ITO/glass substrates (the detailed preparation of the substrates can be found in the supporting information). The spectra (Fig. 1b) displayed an additional

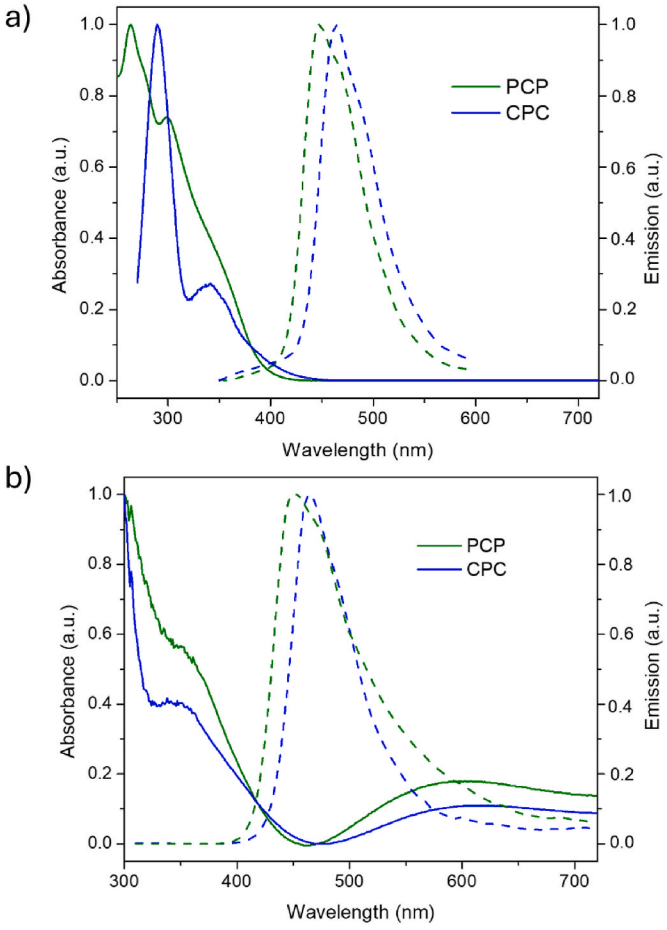

Fig. 1. Absorption and emission spectra of PCP and CPC a) THF solutions and b) spin coated films from THF solutions at 15 mg ml^{-1}. The absorption spectra are shown with solid line, whereas the emission spectra with dashed line with an excitation wavelength of 260 nm for PCP and 280 nm for CPC in solution and set at 290 nm for films.

shoulder for the PCP film around 350 nm and a slightly bathochromic shift of the CPC shoulder, correlated to the increase of π-π stacking [44]. Regarding the fluorescence spectra, the maximum wavelength is slightly shifted between the two molecules, with a value of 455 nm for PCP and 466 nm for CPC, regardless of their aggregation state.

The HOMO levels were determined by cyclic voltammetry (CV) in DCM solution for both molecules (see the supporting information section for the experimental details). The voltammograms (Figure S 8) showed at least three oxidation events. The lowest one was considered to calculate the HOMO level [45]. The opto-electrochemical properties of the molecules are given in Table 1. Both HOMOs are well suited for the use of the considered perovskite, for which the valence band (VB) is at −5.52 eV [29], deeper than the HOMO level of both PCP of −5.33 eV and CPC of −5.22 eV. The LUMO levels were obtained from the HOMO energy and the optical bandgap energy (determined by absorption and emission spectroscopy using the Einstein-Planck relation) [46], which was wider in the case of PCP.

3.3. Computational study

In order to clarify the nature of the electronic transitions, of the large Stokes shift observed for both PCP and CPC, as well as of their electrochemical properties, a computational study was performed based on density functional theory (DFT), including the solvent effects. Such an approach should provide a qualitatively correct description of partial intramolecular charge-transfer electronic states that can show up in large conjugated systems with donor and acceptor units. The most stable conformer of PCP appeared to be the non-symmetrical structure displayed in Fig. 2. The maximum atom-atom distance is 2.1 nm and the overall volume of the molecule computed using van der Waals (VdW) surfaces is about 560 $Å^3$. (Figure S 9). In this structure, the two phenothiazine rings form dihedral angles of 45° and 42° respectively with the central carbazole unit, and are both highly non-planar with a dihedral angle between the two planes defined by the phenyl rings of about 30°. Other conformers with different values of the carbazole-phenothiazine dihedral angle have slightly higher energies. Both absorption and emission spectra are reproduced with reasonable accuracy, considering the calculation level. The computed absorption energies of the three most intense transitions are reported in Table 2, with the maximum intensity transition at 276 nm, which is very close to the experimental value of 263 nm. The peak observed around 300 nm can be associated with the S0- > S4 transition computed around 285 nm, with a significant transition strength. Finally, the computed S0- > S1 transition wavelength is 323 nm, while experimentally, this transition is visible as a low intensity shoulder around 340 nm.

Difference density analysis, displayed in Fig. 2, shows that the S0- > S1 transition is mostly a local excitation involving one phenothiazine ring, the S0- > S4 transition is mostly a CT process between the two phenothiazine rings, while the most intense transition at 276 nm is a local excitation of the carbazole moiety. TDDFT analysis also predicts an emission maximum at 423 nm, which is very close to the observed maximum of 447 nm. The large bathochromic shift observed in the emission is associated with a planarization of the of the S atom in one thiazine ring, which causes a strong localization of the HOMO and LUMO orbitals on the phenothiazine.

In the case of CPC, the maximum atom-atom distance is 2.3 nm, and the overall volume from VdW surfaces is about 540 $Å^3$ (Figure S 10). Likewise PCP, the phenothiazine moiety is highly non-planar, with the two phenyl rings forming an angle of about 30° and the dihedral between the carbazole and the phenothiazine units of 46° and 42°. However, the carbazole units remain completely planar. The three most intense electronic transitions and their emission wavelengths are reported in Table 3 and Fig. 3. Again, both S0- > S1 and S0- > S4 transitions involve mostly the phenothiazine ring, whereas a low intensity transition involving mostly the carbazole moiety is predicted at 258 nm. The experimentally observed peak at 289 nm can be safely assigned to the S0- > S4 transition.

TDDFT calculations also predict a large Stokes shift with the S1- > S0 emission falling at 420 nm. As for PCP, the emission involves almost exclusively the phenothiazine moiety and the Stokes shift is associated with an increased planarity of the molecule in the S1 state.

The computed HOMO level of PCP is −4.943 eV, while that of CPC is −4.889 eV. Both values have been obtained using SMD models of dichloromethane solvent and neglecting vibrational contributions [47].

The errors on the absolute values of HOMO levels are around 350 meV, which is in line with previously reported studies on similar materials [48]. The difference between the two theoretical oxidation potentials is 54 meV, which is in qualitative agreement with the experimental value of 100 meV. This supports the robustness of our results.

3.4. Characterization in devices

3.4.1. General screening of the HTMs

The hole mobilities of PCP and CPC were measured by preparing organic field-effect transistors (OFETs), from THF solutions at a concentration of 15 mg ml^{-1} (leading to a thickness of 40 nm by spin-coating) and low values were obtained from 5.3 × 10^{-8} to 3.6 × 10^{-7} cm^2. $V^{-1}s^{-1}$ (see supporting information). Hence, the inverted architecture was preferred to implement the HTMs in PSCs as lower thicknesses of HTL can be used in the final devices.

Planar inverted p-i-n type PSCs (Fig. 4a) were produced with the following composition: ITO/HTM/$Cs_{0.17}FA_{0.83}Pb(I_{0.80}Br_{0.20})_3$/$PC_{61}BM$/BCP/Cu. A complete description of the device preparation can be found in the supporting information. Upon processing, the perovskite layer had a 422 ± 16 nm thickness and a bandgap of 1.67 eV. The electron transporting layer consisted of phenyl-C_{61}-butyl ester ($PC_{61}BM$) with an interlayer of bathocuproine (BCP), which avoids the direct

Table 1
Electronical and optical properties of both HTM molecules.

HTM	Absorption [nm]		ε at λ_{max}	Emission [nm]		Eg[c]	HOMO	LUMO
	λ_{max}, sol.[a]	λ_{max}, film[b]	($M^{-1}cm^{-1}$)	λ_{max}, sol.	λ_{max}, film	(eV)	(eV)	(eV)
PCP	263.5	–	82000	447	454	3.16	−5.33	−2.14
CPC	289.5	–	82900	464	465	2.97	−5.22	−2.25

[a] Absorbance in THF solution.
[b] The maximum absorbance in film cannot be determined, as the noise of the analysis is too high below 300 nm.
[c] Optical bandgap.

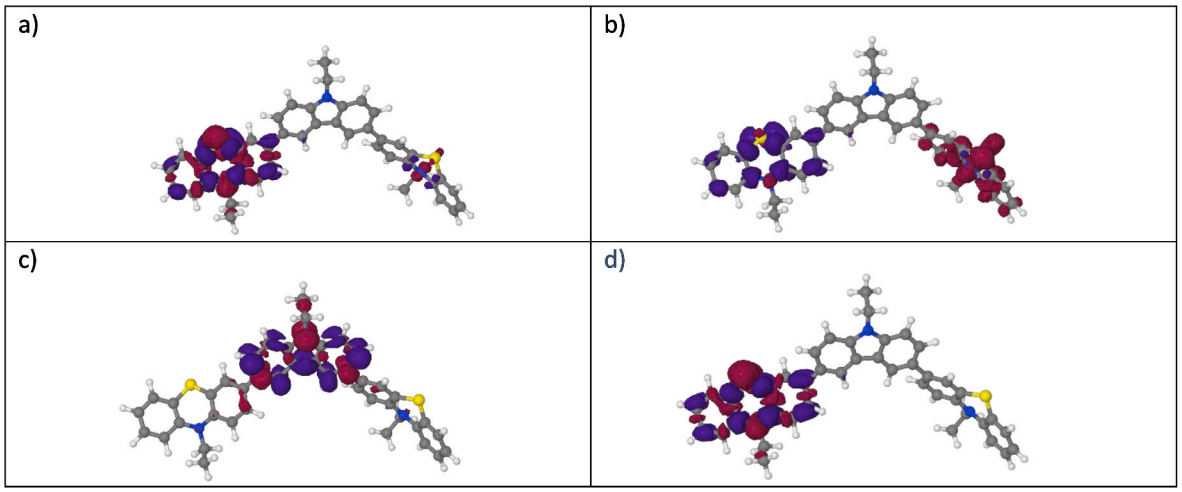

Fig. 2. TD-DFT difference density between PCP ground state and the three excited states with the largest transition strength: a) S0-S1 b) S0-S4, c) S0-S6, d) TD-DFT difference density between the ground state and the first excited state at the geometry optimized for the S1 emission. The isosurfaces were plotted with a cutoff value of ± 0.002.

Table 2
Analysis of the main transitions of PCP.

Transition assignment	Abs. wavelength (nm)	Oscillator strength
S0- > S1	324	0.21
S0- > S4	285	0.38
S0- > S6	276	0.77
S1- > S0 (emission)	426	0.07

Table 3
Analysis of the main transitions of CPC.

Orbital contribution	Abs. wavelength (nm)	Oscillator strength
S0- > S1	321	0.32
S0- > S4	277	0.78
S0- > S6	258	0.10
S1- > S0 (emission)	420	0.22

contact between $PC_{61}BM$ and Cu and ensures the proper flow of charges to the corresponding electrode [49]. Fig. 4b and c shows the energetic levels of the materials composing the cells, obtained by optoelectronic characterizations (Fig. 4b) and synchrotron-based PES (Fig. 4c).

A systematic comparison between both HTMs and the reference HTM polymer PTAA was carried out. Furthermore, cells without HTM were prepared to fully understand the beneficial impact of the HTMs on cell efficiency and stability. The initial concentration of the molecules was set at 2 mg ml^{-1} in THF, whereas a solution of PTAA 2 mg ml^{-1} in toluene was used [52,53].

After the deposition of the HTMs layer, the substrates underwent a classical annealing at 100 °C for 10 min, carried out for both molecules and the references. A harsher annealing at 150 °C for 30 min was also tested for PCP and CPC, since both molecules were stable up to 350 °C, as shown by thermogravimetric analysis (TGA) (Figure S 12). The spectroscopic behaviour of the film did not show any remarkable difference upon annealing (see SI, Table S5 and Figure S 14). The resulting photovoltaic parameters, averaged on 12 devices, are summarized in Table 4. Both forward and reverse scans were used as no hysteresis was

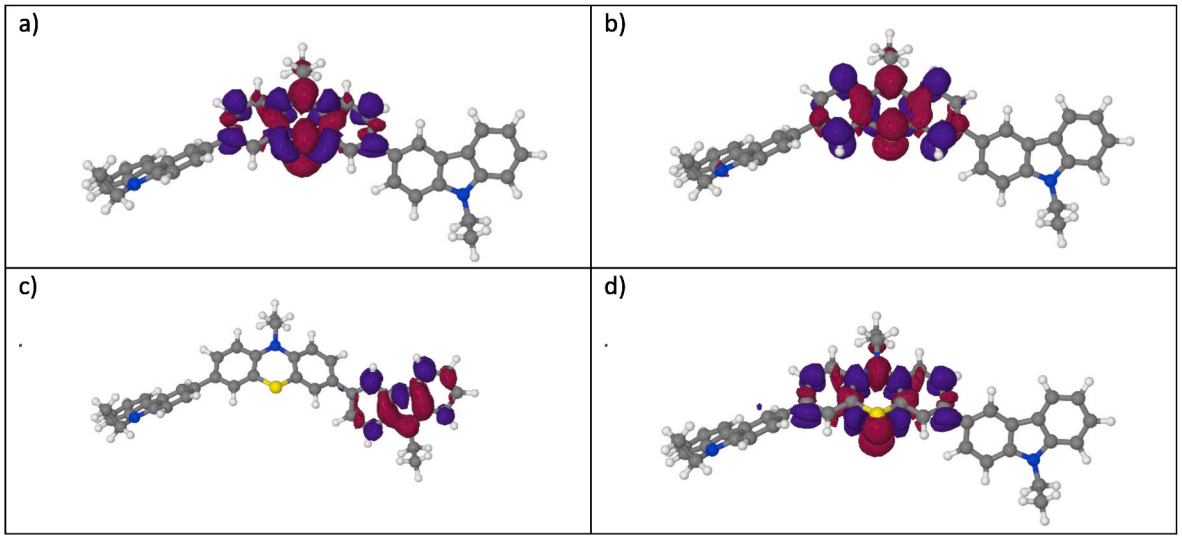

Fig. 3. TD-DFT difference density between the CPC ground state and the two excited states with the largest transition strength: a) S0-S1 b) S0-S4, c) S0-S6, d) TD-DFT difference density between the ground state and the first excited state at the geometry optimized for the S1 emission. The isosurfaces were plotted with a cutoff value of ± 0.002.

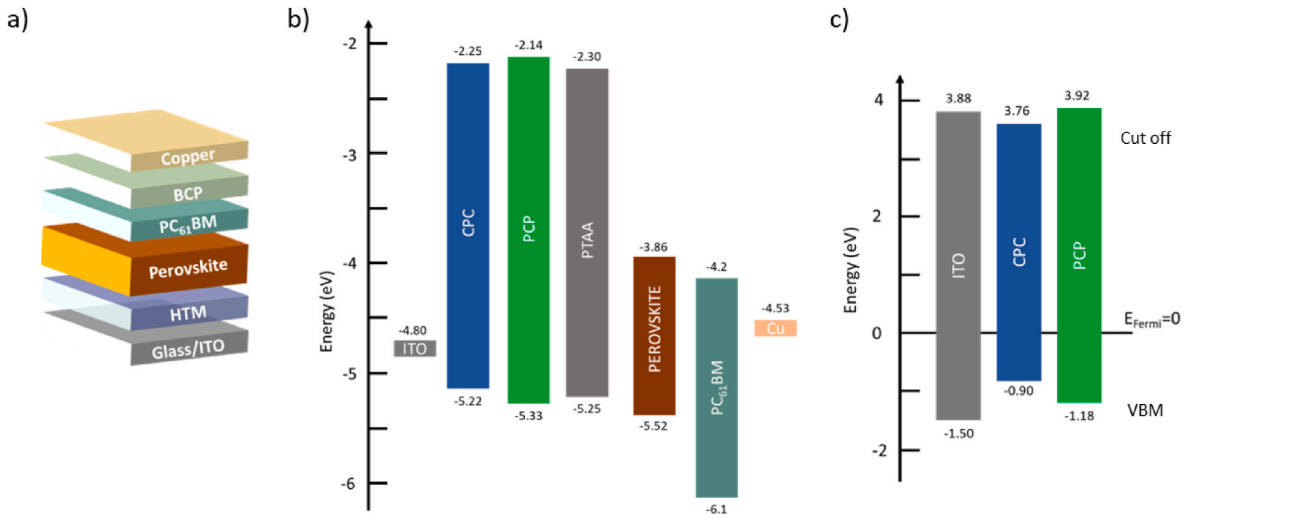

Fig. 4. a) Solar cell architecture. The thicknesses of the layers are the following: 422 nm for the perovskite, 40 nm for $PC_{61}BM$, 8 nm for BCP and 100 nm for copper. b) Energetic levels of HTM and ETM layers, with $E_{VAC} = 0$, HOMO levels were determined by cyclic voltammetry, while LUMO levels through spectroscopy. The value for ITO was taken from Caliò et al., [50] the values of the PTAA reference were taken from the producer website (https://solarischem.com/procurement/ptaa-batch/), the values for $PC_{61}BM$ and BCP were taken from Chen et al. [49] and for copper from Wang et al. [51] c) Energetic levels (work function and Valence Band Maximum) of HTMs and ITO were determined from Secondary electron cut-off and valence band photemission spectra obtained from PES experiments (fig S19 b and c respectively), with $E_F = 0$.

Table 4
Photovoltaic parameters of perovskite solar cells without and in presence of HTMs. All data are averaged on 12 devices using reverse and forward scans as no hysteresis was observed (see SI Figure S 21 for the JV curves of the best devices).

HTM	Annealing	V_{OC} [V]	J_{SC} [mA.cm^{-2}]	FF [%]	PCE [%]
NO HTM		0.51 ± 0.10	15.8 ± 0.9	65.2 ± 9.2	5.3 ± 1.6
PCP	100 °C, 10′	0.97 ± 0.01	17.9 ± 0.2	71.6 ± 2.1	12.5 ± 0.2
	150 °C, 30′	0.93 ± 0.02	18.5 ± 0.3	77.6 ± 1.3	13.4 ± 0.2
CPC	100 °C, 10′	0.74 ± 0.06	13.8 ± 0.6	76.3 ± 1.1	7.8 ± 0.4
	150 °C, 30′	0.85 ± 0.04	11.3 ± 1.0	70.2 ± 8.1	6.7 ± 1.0
PTAA	100 °C, 10′	1.05 ± 0.03	18.2 ± 0.95	76.0 ± 3.7	14.5 ± 1.1

observed on JV curves, see Figure S 21 for the JV curves of the best devices. The presence of a HTL in the solar cells increased PCE from 5.3 % for HTM-free devices to 13.4 % for PCP-based devices, thanks to an important increase in V_{OC} with the insertion of an HTL.

When comparing both molecules, PCP outperforms CPC, especially when the solar cells are annealed at 150 °C. Indeed, PCP-based devices showed higher performances upon this thermal treatment, with a PCE of 13.4 % (against 12.5 % obtained with thermal treatment at 100 °C for 10 min), mainly thanks to an increase in J_{SC}. For CPC, the harshest annealing was slightly detrimental to cell performances, which went from 7.8 % to 6.7 %, due to a decrease of J_{SC}

Besides non-negligible J_{SC} differences, CPC possess a lower V_{OC} (0.74 V against 0.97 V for PCP). As the V_{OC} parameter depends on the difference between the quasi-Fermi levels at the contacts [54], the higher V_{OC} value of PCP can be attributed to its deeper HOMO value. PCP-based devices displayed comparable PCE to the reference PTAA, proving its relevancy as HTL.

High fill factors were achieved for both molecules, which are actually higher than that of the PTAA reference in the same optimal conditions, and above 76 %. It is important to emphasize that, in many cases, lower fill factors are obtained when dopant-free HTMs are employed [50]. As FF is highly affected by parasitic losses (like series resistances) and by interfacial charges recombination due to an inefficient charge extraction or current leakage [55–57], it appears that PCP and CPC are good HTM candidates thanks to their ability to efficiently extract the charges generated by the perovskite.

The solid-state organization of the molecules was evaluated by Wide Angle X-ray Scattering. Both molecules present an amorphous structure, regardless of temperature (Figure S 15). These results are consistent with DSC thermograms that only showed a glass transition temperature around 60 °C, probably related to the alkyl chains (Figure S 13). However, a long-range organization was observed for PCP compound, as an extra broad peak at about q ~ 0.1 Å^{-1} was identified. This structural feature is consistent with the improved optoelectronic properties observed for PCP.

A good matching of the energy levels and work functions at the layers interfaces in the devices is crucial to achieve an efficient extraction and collection of the generated charges. Matching the valence band/HOMO of the electrode/hole transporting layer with the valence band of the perovskite allows to maximize the V_{OC}, which is lowered by charge recombination (due to inefficient charge collection) and narrows bandgap [58,59]. Indeed, an energetic levels modification is often attributed to electronic disturbance created by a thin layer of an organic molecule deposited at the surface of the electrode [60], and several studies showed their influence on the device efficiencies [61–63]. Ultraviolet Photoelectron Spectroscopy (UPS) was carried out to probe the valence band maximum (VBM) and work function (WF) of the ITO electrode modified with PCP and CPC. An analysis of Secondary electron cut-off and valence band photoemission spectra measured with soft X-rays having an energy of 60 eV allowed to determine the VBM and WF of the samples, and all spectra were plotted with respect to the Fermi level measured on a referenced gold substrate. All spectra and experimental procedures are available in supporting information (Figure S16-S19). After modification with the HTM, the secondary

electron cut-off position of ITO is shifted by - 0.128 and + 0.034 eV for CPC and PCP, respectively (Figure S19 c). The higher work function in the presence of PCP is beneficial for the hole transport [58,61,63–65]. Indeed, it leads to a better ohmic contact between the electrode and the perovskite, and thus, a facilitated electron transfer, explaining the higher V_{oc} obtained when PCP is used as HTL compared to CPC. Fig. 4c shows the energetic diagram of the solar cell component with the WF and VBM measured for CPC and PCP modified ITO. A direct comparison between the energetic values obtained through synchrotron-based analysis and the CB and VB of the PSK is not possible, as the instrumental set up was different among the various measurements. Finally, no preferential orientation of π-conjugated CPC or PCP molecules adsorbed on the ITO surface was determined with the use of Near-Edge X-ray Absorption Fine Structure (NEXAFS), as shown in Figure S20 [66,67].

3.4.2. Study of the HTM concentration and stability of the materials

The concentration of the HTM solutions was decreased to 1 and 0.5 mg ml^{-1} to investigate the effect of thinner films. Indeed, the thickness of the HTL, tuned by the concentration of the used solution and the spin coating speed [68], heavily influences the performances the solar cells. Moreover, it could balance the low hole mobilities measured in OFETs. To study the concentration effect, the thermal annealing at 150 °C for 30' has been kept for both molecules.

Upon decreasing the concentration to 1 and 0.5 mg ml^{-1} for both molecules, a slight improvement of performances was achieved for PCP, while a strong increase was observed for CPC (Table 5). Indeed, PCE of PCP was improved from 13.4 % to 14.1 % (14.5 % for champion device), thanks to a slight increase of J_{SC} and FF (18.2 mA cm^{-2} and 81.7 %, respectively for champion device). For CPC, a more significant improvement was obtained, starting from a PCE of 6.7 % at 2 mg ml^{-1}, up to 10.37 % at 0.5 mg ml^{-1}. Whereas the V_{OC} remained constant at around 0.84 V in all cases, the lowering of concentration allowed higher J_{SC} and FF (16.3 mA cm^{-2} and 81.9 %, respectively for champion device). Anyway, the low V_{OC} and J_{SC} represent critical factors that still need to be overcome.

The JV curves of the cells based on both molecules at the lowest concentration of 0.5 mg ml^{-1} are presented in Fig. 5a. It is worth noting that similar JV curves are obtained upon forward and reverse bias, still indicating the absence of hysteresis. Incident Photon-to-Current Efficiency (IPCE) experiments (Fig. 5b and Figure S 22) were carried out on the most efficient devices (one for each HTM, including the reference) to investigate the dependence of the photocurrent produced on the irradiation wavelengths. The IPCE of the PCP-based best device is only slightly lower than that of the PTAA (Fig. 5b) and displayed a high contribution of about 80 % throughout the visible spectrum. In the case of CPC, IPCE is lower than that of PCP with a value about 70 %. The lower CPC photogenerated current may be correlated to a lower absorption behaviour, as clearly observed in UV–visible spectra of thin films prepared from the same solution concentration (see Fig. 1b).

To have a deeper understanding of the concentration effect on device performances, the charge carrier features were investigated by transient photocurrent (TPC) and transient photovoltage (TPV). TPC gives insights into the charge extraction dynamics whereas TPV allows to measure the charge carrier density [69]. TPC was carried out in a high perturbation regime, which means that the cell went from dark to a specific illumination set by a light emitting diode (LED) source. The cell was kept in the short-circuit condition during the entire measurement. No substantial differences in the charge extraction properties were found changing the concentration of the PCP solution (see Figure S 23 a). In contrast, slightly better properties could be obtained with the CPC solution at the lowest concentration (Figure S 23 c). TPV measurements were performed as well in a small perturbation regime. The cell was kept at open circuit, with a specific background illumination applied from the LED source. Then, a small overcurrent was sent to the LED to create a voltage perturbation (20 mV), with a decay that was subsequently monitored. TPV analysis for PCP-based devices underlined a longer recombination time when using the 0.5 mg ml^{-1} solution at low light bias, and at high light intensity shows the advantage of using lower concentrations (0.5 and 1 mg ml^{-1}) instead of a higher one (2 mg ml^{-1}) (Figure S 23 b). When analyzing CPC-based devices, TPV analysis enlightened that at medium light intensity (0.7 V), the recombination times are longer for 0.5 mg ml^{-1}, whereas the results became similar at high voltage (high light intensity) (Figure S 23 d). These results giving insights in charge carrier dynamics upon the decrease of HTM concentration show a more significant improvement for CPC. This positive effect is in good agreement to the effect observed on devices performances.

To confirm the results obtained by TPV analysis, we performed steady state and Time Resolved Photoluminescence (TRPL) measurements by comparing PCP and CPC based samples consisting of Glass/PCP (or CPC)/$Cs_{0.17}FA_{0.83}Pb(I_{0.80}Br_{0.20})_3$. The increase in steady-state PL intensity for PCP-based sample, compared to CPC, demonstrates a significant reduction in non-radiative recombination (Figure S 24a). This improvement in steady-state PL intensity is indicative of enhanced radiative recombination pathways. Moreover, the carrier lifetime measured by TRPL analysis in PCP-based sample is significantly longer than that in CPC-based sample, suggesting that even non-radiative recombination processes are reduced using PCP molecule due to enhanced interface quality and reduced surface recombination (Figure S 24b) [70].

Finally, to assess the shelf-life stability of both HTMs after one year, we have fabricated devices with them (with the optimized parameters), compared again with our PTAA reference. It has been found that the molecules are quite stable given that they were stored outside the glovebox; they are easily reproduced with out-of-glovebox storage for more than one year. The comparison of the device performances is shown in supplementary information (Figure S 25).

Table 5
Photovoltaic parameters of the cells made using different HTMs concentrations (after annealing at 150 °C for 30'). All data are an average of reverse and forward scans.

HTM	[mg.ml^{-1}]	V_{OC} [V]	J_{SC} [mA.cm^{-2}]	FF [%]	PCE [%]
PCP	2	0.93 ± 0.02	18.5 ± 0.3	77.6 ± 1.3	13.4 ± 0.2
	1	0.94 ± 0.02	18.9 ± 0.2	79.7 ± 1.5	14.1 ± 0.2
	0.5	0.95 ± 0.04	18.7 ± 0.8	78.8 ± 3.2	14.0 ± 0.7
CPC	2	0.85 ± 0.04	11.3 ± 1.0	70.2 ± 8.1	6.7 ± 1.0
	1	0.84 ± 0.04	13.8 ± 1.0	75.4 ± 4.9	8.8 ± 0.7
	0.5	0.83 ± 0.03	15.8 ± 0.5	78.5 ± 4.2	10.4 ± 0.8

4. Conclusion

The two molecules PCP and CPC were synthesized in five steps, with optimized procedures to increase the overall yield of production whenever possible. Optoelectronic properties being first characterized and compared with DFT calculations, they were then implemented in inverted p-i-n devices, using $Cs_{0.17}FA_{0.83}Pb(I_{0.80}Br_{0.20})_3$. Comparable efficiencies to the PTAA reference were achieved in optimized conditions for PCP, and slightly lower for CPC. PCP-based devices showed an average PCE of 14.1 % with a champion cell of 14.5 %. For PCP, the annealing procedure was found to be decisive to increase J_{SC}, while the decrease of HTM concentration played an important role for CPC-based devices, allowing to reach a PCE of 10.4 %. Advanced characterizations were performed to investigate the performance difference for both HTMs. PES analyses enabled to explain this as remarkable differences in the electronic behaviour and the work-function modifications were revealed by the Secondary electron cut-off photoemission spectra analysis. After modification with the HTM, the secondary electron cut-off position of ITO showed a higher work function in presence of PCP, beneficial for the hole transport and ohmic contact between the

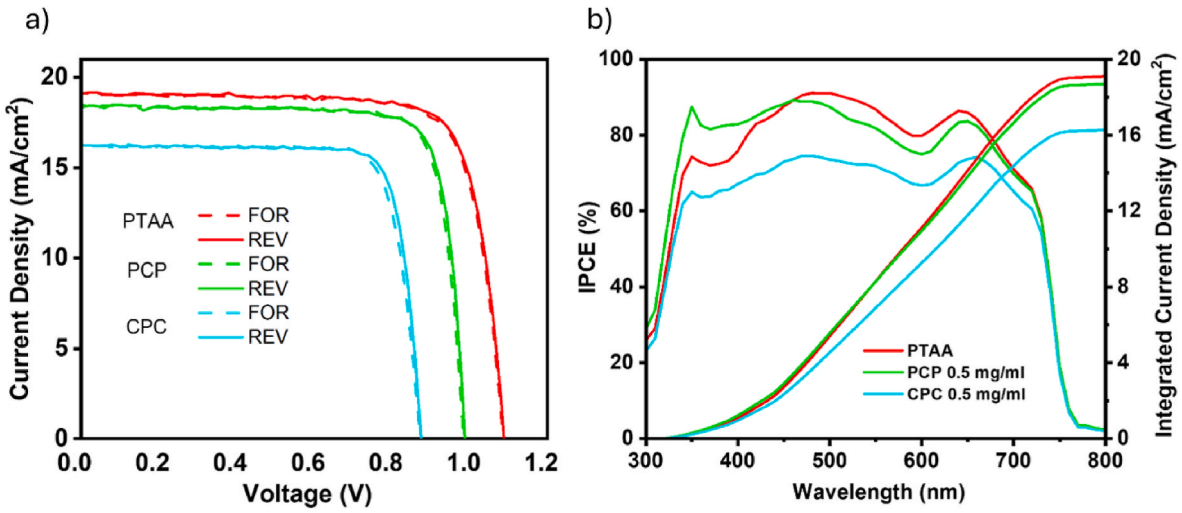

Fig. 5. a) JV and b) IPCE analysis of the best pixel at the concentration of 0.5 mg ml^{-1} of the HTMs. In JV curves, forward scans (solid lines) and reverse scans (dashed lines) are indicated.

electrode and the perovskite. As complementary experiments, transient photocurrent and transient photovoltage measurements were performed at various HTM concentrations. While TPC on PCP did not show a significant improvement upon concentration decrease, TPC on CPC clearly demonstrates its positive effect, indicating a better charge carrier dynamics. By TPV, both HTMs displayed longer recombination times for the lowest concentration, once again in agreement with device results. Moreover, results from UV–visible absorption in thin films and WAXS experiments indicated more suitable properties for PCP, with a higher absorption and a long-range organization, respectively. Finally, steady state PL and time resolved PL also confirmed more favourable features for PCP, with a significant reduction of non-radiative recombination and higher carrier lifetimes.

The present work highlights the importance of the molecular design on the material performances upon device implementation. We observed how the same starting scaffolds differently assembled in the final material led to different performances, explained by a different electronic behaviour. Both molecules demonstrated to be suitable as potential low-cost HTMs for perovskite solar cells when implemented in inverted devices and were found stable under air storage after one year.

CRediT authorship contribution statement

Valentina Maruzzo: Writing – review & editing, Writing – original draft, Visualization, Investigation, Formal analysis, Conceptualization. **Antoine Bousquet:** Writing – review & editing, Writing – original draft, Supervision, Project administration, Investigation, Conceptualization. **Fabio Matteocci:** Writing – original draft, Supervision. **Elisa Nonni:** Investigation. **Daimiota Takhellambam:** Writing – original draft, Investigation. **Raffaele Borrelli:** Writing – original draft, Investigation. **Damiano Mangatia:** Writing – original draft, Investigation. **Eric Grelet:** Writing – original draft, Investigation. **Mamatimin Abbas:** Writing – original draft, Investigation. **Mathieu G. Silly:** Writing – original draft, Investigation, Writing – review & editing. **Matteo Bonomo:** Writing – original draft, Investigation, Conceptualization. **Aldo Di Carlo:** Resources, Project administration. **Claudia Barolo:** Funding acquisition, Conceptualization. **Nadia Barbero:** Supervision, Resources, Project administration, Funding acquisition, Conceptualization. **Christine Lartigau-Dagron:** Writing – review & editing, Writing – original draft, Supervision, Resources, Project administration, Funding acquisition, Conceptualization.

Declaration of competing interest

The authors declare the following financial interests/personal relationships which may be considered as potential competing interests: University of Pau and Pays de l'Adour reports financial support and article publishing charges were provided by University of Pau and Pays de l'Adour. If there are other authors, they declare that they have no known competing financial interests or personal relationships that could have appeared to influence the work reported in this paper.

Funding/Acknowledgements

The authors thank UNITA alliance and UPPA for the funding of VM, the Grant for Internationalization (GFI), Programmazione Triennale 21–23, "Green technologies: renewable energies and the green transition". The authors also acknowledge support from Project CH4.0 under the MUR program "Dipartimenti di Eccellenza 2023–2027" (CUP: D13C22003520001). VM acknowledges the Vinci project 2023 - Chapitre 2 (project number: C2-168) and VIPERLAB project VLAB-211-00029. CLD acknowledges the VIPERLAB project VLAB-222-00057.

Appendix A. Supplementary data

Supplementary data to this article can be found online at https://doi.org/10.1016/j.solmat.2025.113697.

Data availability

Data will be made available on request.

References

[1] NREL, Best Research-Cell Efficiency Chart, november 2023.
[2] S. Khatoon, S. Kumar Yadav, V. Chakravorty, J. Singh, R. Bahadur Singh, M. S. Hasnain, et al., Perovskite solar cell's efficiency, stability and scalability: a review, Mater. Sci. Energy Technol. 6 (2023) 437–459, https://doi.org/10.1016/j.mset.2023.04.007.
[3] P. Basumatary, P. Agarwal, A short review on progress in perovskite solar cells, Mater. Res. Bull. 149 (2022) 111700, https://doi.org/10.1016/j.materresbull.2021.111700.
[4] J. Yang, X. Luo, Y. Zhou, Y. Li, Q. Qiu, T. Xie, Recent advances in inverted perovskite solar cells: designing and fabrication, Int. J. Mol. Sci. 23 (2022) 39, https://doi.org/10.3390/ijms231911792.
[5] S. Wang, Z. Huang, X. Wang, Y. Li, M. Gunther, S. Valenzuela, et al., Unveiling the role of tBP-LiTFSI complexes in perovskite solar cells, J. Am. Chem. Soc. 140 (2018) 16720–16730, https://doi.org/10.1021/jacs.8b09809.

[6] F.M. Rombach, S.A. Haque, T.J. Macdonald, Lessons learned from spiro-OMeTAD and PTAA in perovskite solar cells, Energy Environ. Sci. 14 (2021) 5161–5190, https://doi.org/10.1039/d1ee02095a.
[7] Y. Yao, C. Cheng, C. Zhang, H. Hu, K. Wang, S. De Wolf, Organic hole-transport layers for efficient, stable, and scalable inverted perovskite solar cells, Adv. Mater. 34 (2022) e2203794, https://doi.org/10.1002/adma.202203794.
[8] R. Zhu, Inverted devices are catching up, Nat. Energy 5 (2020) 123–124, https://doi.org/10.1038/s41560-020-0559-z.
[9] K. Rakstys, C. Igci, M.K. Nazeeruddin, Efficiency vs. stability: dopant-free hole transporting materials towards stabilized perovskite solar cells, Chem. Sci. 10 (2019) 6748–6769, https://doi.org/10.1039/c9sc01184f.
[10] C. Zhang, Q. Liao, J. Chen, B. Li, C. Xu, K. Wei, et al., Thermally crosslinked hole conductor enables stable inverted perovskite solar cells with 23.9% efficiency, Adv. Mater. 35 (2023) 2209422, https://doi.org/10.1002/adma.202209422.
[11] S. Wang, H. Guo, Y. Wu, Advantages and challenges of self-assembled monolayer as a hole-selective contact for perovskite solar cells, Mater. Futures 2 (2023), https://doi.org/10.1088/2752-5724/acbb5a.
[12] D. Pan, D.L. Phillips, Raman and density functional study of the S0 state of phenothiazine and the radical cation of phenothiazine, J. Phys. Chem. 103 (1999) 4737–4743, https://doi.org/10.1021/jp990399h.
[13] K.S. Keremane, R. Rao, A.V. Adhikari, Simple 3,6-disubstituted carbazoles as potential hole transport materials: photophysical, electrochemical and theoretical studies, Photochem. Photobiol. 97 (2021) 289–300, https://doi.org/10.1111/php.13337.
[14] K. Radhakrishna, S.B. Manjunath, D. Devadiga, R. Chetri, A.T. Nagaraja, Review on carbazole-based hole transporting materials for perovskite solar cell, ACS Appl. Energy Mater. 6 (2023) 3635–3664, https://doi.org/10.1021/acsaem.2c03025.
[15] C. Rodríguez-Seco, L. Cabau, A. Vidal-Ferran, E. Palomares, Advances in the synthesis of small molecules as hole transport materials for lead halide perovskite solar cells, Acc. Chem. Res. 51 (2018) 869–880, https://doi.org/10.1021/acs.accounts.7b00597.
[16] I.J. Al-Busaidi, A. Haque, N.K. Al Rasbi, M.S. Khan, Phenothiazine-based derivatives for optoelectronic applications: a review, Synth. Met. (2019) 257, https://doi.org/10.1016/j.synthmet.2019.116189.
[17] R. Grisorio, B. Roose, S. Colella, A. Listorti, G.P. Suranna, A. Abate, Molecular tailoring of phenothiazine-based hole-transporting materials for high-performing perovskite solar cells, ACS Energy Lett. 2 (2017) 1029–1034, https://doi.org/10.1021/acsenergylett.7b00054.
[18] M. Zhai, Y. Miao, C. Chen, L. Liu, H. Wang, X. Ding, et al., Modulating donor assemblies of D-π-D type hole transport materials for perovskite solar cells, J. Power Sources 551 (2022) 232199, https://doi.org/10.1016/j.jpowsour.2022.232199.
[19] J. Luo, F. Han, Z. Wan, H.A. Malik, B. Zhao, L. Chen, et al., Structure-performance relationships of hole-transporting materials in perovskite solar cells: minor structural discrepancy effects on the efficiency, Electrochim. Acta 257 (2017) 380–387, https://doi.org/10.1016/j.electacta.2017.10.085.
[20] J.-H. Chen, K.-M. Lee, C.-C. Ting, C.-Y. Liu, Step-saving synthesis of star-shaped hole-transporting materials with carbazole or phenothiazine cores via optimized C-H/C-Br coupling reactions, RSC Adv. 11 (2021) 8879–8885, https://doi.org/10.1039/d0ra10190g.
[21] S. Lengvinaite, J.V. Grazulevicius, V. Jankauskas, S. Grigalevicius, Carbazole-based aromatic amines having oxetanyl groups as materials for hole transporting layers, Synth. Met. 157 (2007) 529–533, https://doi.org/10.1016/j.synthmet.2007.05.015.
[22] M. Li, Z. Wang, M. Liang, L. Liu, X. Wang, Z. Sun, et al., Low-cost carbazole-based hole-transporting materials for perovskite solar cells: influence of S,N-heterocycle, J. Phys. Chem. C 122 (2018) 24014–24024, https://doi.org/10.1021/acs.jpcc.8b09482.
[23] P. Huang, Kazim S. Manju, L. Lezama, R. Misra, S. Ahmad, Tailoring of a phenothiazine core for electrical conductivity and thermal stability: hole-selective layers in perovskite solar cells, ACS Appl. Mater. Interfaces 13 (2021) 33311–33320, https://doi.org/10.1021/acsami.1c08470.
[24] F. Zhang, S. Wang, H. Zhu, X. Liu, H. Liu, X. Li, et al., Impact of peripheral groups on phenothiazine-based hole-transporting materials for perovskite solar cells, ACS Energy Lett. 3 (2018) 1145–1152, https://doi.org/10.1021/acsenergylett.8b00395.
[25] R. Wang, Z. Gong, Y. Jiang, S. Huang, B. Liu, G. Zhou, et al., Low-cost planar organic small molecules as hole transport materials for high efficient perovskite solar cells, Surf. Interfaces 34 (2022), https://doi.org/10.1016/j.surfin.2022.102307.
[26] W. Li, H. Dong, L. Wang, N. Li, X. Guo, J. Li, et al., Montmorillonite as bifunctional buffer layer material for hybrid perovskite solar cells with protection from corrosion and retarding recombination, J. Mater. Chem. A 2 (2014) 13587–13592, https://doi.org/10.1039/C4TA01550A.
[27] T. Leijtens, T. Giovenzana, S.N. Habisreutinger, J.S. Tinkham, N.K. Noel, B. A. Kamino, et al., Hydrophobic organic hole transporters for improved moisture resistance in metal halide perovskite solar cells, ACS Appl. Mater. Interfaces 8 (2016) 5981–5989, https://doi.org/10.1021/acsami.5b10093.
[28] A. Magomedov, E. Kasparavičius, K. Rakstys, S. Paek, N. Gasilova, K. Genevičius, et al., Pyridination of hole transporting material in perovskite solar cells questions the long-term stability, J. Mater. Chem. C 6 (2018) 8874–8878, https://doi.org/10.1039/C8TC02242A.
[29] F. Hou, Y. Li, L. Yan, B. Shi, N. Ren, P. Wang, et al., Control perovskite crystals vertical growth for obtaining high-performance monolithic perovskite/silicon heterojunction tandem solar cells with VOC of 1.93 V, Sol. RRL 5 (2021) 2100357, https://doi.org/10.1002/solr.202100357.
[30] F. Polack, M. Silly, C. Chauvet, B. Lagarde, N. Bergeard, M. Izquierdo, et al., TEMPO: a new insertion device beam line at SOLEIL for time resolved photoelectron spectroscopy experiments on solids and interfaces, in: 10th International Conference on Synchrotron Radiation Instrumentation, AIP Conference Proceedings, Melbourne, AUSTRALIA, 2010, pp. 185–188, https://doi.org/10.1063/1.3463169.
[31] N. Bergeard, M.G. Silly, D. Krizmancic, C. Chauvet, M. Guzzo, J.P. Ricaud, et al., Time-resolved photoelectron spectroscopy using synchrotron radiation time structure, J. Synchrotron Radiat. 18 (2011) 245–250, https://doi.org/10.1107/s0909049510052301.
[32] J.-D. Chai, M. Head-Gordon, Long-range corrected hybrid density functionals with damped atom–atom dispersion corrections, Phys. Chem. Chem. Phys. 10 (2008) 6615–6620, https://doi.org/10.1039/B810189B.
[33] F. Neese, Software update: the ORCA program system—version 5.0, WIREs Comput. Mol. Sci. 12 (2022) e1606, https://doi.org/10.1002/wcms.1606.
[34] J. Wang, Y. Lu, W. McCarthy, R. Conway-Kenny, B. Twamley, J. Zhao, et al., Novel ruthenium and iridium complexes of N-substituted carbazole as triplet photosensitisers, Chem. Commun. 54 (2018) 1073–1076, https://doi.org/10.1039/c7cc08535d.
[35] N. Altinolcek, A. Battal, M. Tavasli, W.J. Peveler, H.A. Yu, P.J. Skabara, Synthesis of novel multifunctional carbazole-based molecules and their thermal, electrochemical and optical properties, Beilstein J. Org. Chem. 16 (2020) 1066–1074, https://doi.org/10.3762/bjoc.16.93.
[36] L.S. Coumont, J.G.C. Veinot, Ni(COD)2 coupling of 3,6-dibromocarbazoles as a route to all-carbazole shape persistent macrocycles, Tetrahedron Lett. 56 (2015) 5595–5598, https://doi.org/10.1016/j.tetlet.2015.08.048.
[37] M.M.H. Desoky, F. Cruciani, P. Quagliotto, G. Viscardi, Synthesis and characterization of transparent phenothiazine-based polymers via buchwald-hartwig polymerization as promising functional organic materials, J. Mol. Struct. (2024), https://doi.org/10.1016/j.molstruc.2024.137635.
[38] Y. Jiaoa, L. Mao, S. Liua, T. Tan, D. Wang, D. Cao, et al., Effects of meta or para connected organic dyes for dye-sensitized solar cell, Dyes Pigments (2018), https://doi.org/10.1016/j.dyepig.2018.05.037.
[39] M. Sailer, A.W. Franz, T.J. Muller, Synthesis and electronic properties of monodisperse oligophenothiazines, Chemistry 14 (2008) 2602–2614, https://doi.org/10.1002/chem.200701341.
[40] C. Yin, H. Zhu, C. Xie, L. Zhang, P. Chen, Q. Fan, et al., Organic nanoprobe cocktails for multilocal and multicolor fluorescence imaging of reactive oxygen species, Adv. Funct. Mater. 27 (2017), https://doi.org/10.1002/adfm.201700493.
[41] S. Aghazada, Y. Ren, P. Wang, M.K. Nazeeruddin, Effect of donor groups on the performance of cyclometalated ruthenium sensitizers in dye-sensitized solar cells, Inorg. Chem. 56 (2017) 13437–13445, https://doi.org/10.1021/acs.inorgchem.7b02164.
[42] M. Mao, X.-L. Zhang, X.-Q. Fang, G.-H. Wu, S.-Y. Dai, Q.-H. Song, et al., Highly efficient light-harvesting boradiazaindacene sensitizers for dye-sensitized solar cells featuring phenothiazine donor antenna, J. Power Sources 268 (2014) 965–976, https://doi.org/10.1016/j.jpowsour.2014.05.079.
[43] S. Wang, H. Wang, J. Guo, H. Tang, J. Zhao, Influence of the terminal electron donor in D–D–π–A phenothiazine dyes for dye-sensitized solar cells, Dyes Pigments 109 (2014) 96–104, https://doi.org/10.1016/j.dyepig.2014.05.015.
[44] S. Benhattab, R. Nakar, J.W. Rodriguez Acosta, N. Berton, J. Faure-Vincent, J. Bouclé, et al., Carbazole-based twin molecules as hole-transporting materials in dye-sensitized solar cells, Dyes Pigments 151 (2018) 238–244, https://doi.org/10.1016/j.dyepig.2017.12.050.
[45] G.P. Kissling, B. Ruhstaller, K.P. Pernstich, Measuring frontier orbital energy levels of OLED materials using cyclic voltammetry in solution, Org. Electron. 122 (2023), https://doi.org/10.1016/j.orgel.2023.106888.
[46] A.A. Adeniyi, T.L. Ngake, J. Conradie, Cyclic voltammetric study of 2-hydroxybenzophenone (HBP) derivatives and the correspondent change in the orbital energy levels in different solvents, Electroanalysis 32 (2020) 2659–2668, https://doi.org/10.1002/elan.202060163.
[47] J. Ho, Are thermodynamic cycles necessary for continuum solvent calculation of pKas and reduction potentials? Phys. Chem. Chem. Phys. 17 (2015) 2859–2868, https://doi.org/10.1039/c4cp04538f.
[48] S. Naqvi, A. Patra, Hole transport materials for perovskite solar cells: a computational study, Mater. Chem. Phys. 258 (2021), https://doi.org/10.1016/j.matchemphys.2020.123863.
[49] C. Chen, S. Zhang, S. Wu, W. Zhang, H. Zhu, Z. Xiong, et al., Effect of BCP buffer layer on eliminating charge accumulation for high performance of inverted perovskite solar cells, RSC Adv. 7 (2017) 35819–35826, https://doi.org/10.1039/c7ra06365b.
[50] L. Calio, S. Kazim, M. Gratzel, S. Ahmad, Hole-transport materials for perovskite solar cells, Angew Chem. Int. Ed. Engl. 55 (2016) 14522–14545, https://doi.org/10.1002/anie.201601757.
[51] L. Wang, G.-R. Li, Q. Zhao, X.-P. Gao, Non-precious transition metals as counter electrode of perovskite solar cells, Energy Storage Mater. 7 (2017) 40–47, https://doi.org/10.1016/j.ensm.2016.11.007.
[52] Y. Li, B. Wang, T. Liu, Q. Zeng, D. Cao, H. Pan, et al., Interfacial engineering of PTAA/perovskites for improved crystallinity and hole extraction in inverted perovskite solar cells, ACS Appl. Mater. Interfaces 14 (2022) 3284–3292, https://doi.org/10.1021/acsami.1c21000.
[53] L.A. Castriotta, R. Infantino, L. Vesce, M. Stefanelli, A. Dessì, C. Coppola, et al., Stable methylammonium-free p-i-n perovskite solar cells and mini-modules with phenothiazine dimers as hole-transporting materials, Energy Environ. Mater. 6 (2023), https://doi.org/10.1002/eem2.12455.

[54] K.S. Keremane, A.V. Adhikari, Simple carbazole derivatives with mono/dimethoxyphenylacrylonitrile substituents as hole-transporting materials: performance studies in hybrid perovskite solar cells, Electrochem. Sci. Adv. 1 (2021), https://doi.org/10.1002/elsa.202000036.
[55] N. Wu, Y. Wu, D. Walter, H. Shen, T. Duong, D. Grant, et al., Identifying the cause of voltage and fill factor losses in perovskite solar cells by using luminescence measurements, Energy Technol. 5 (2017) 1827–1835, https://doi.org/10.1002/ente.201700374.
[56] C. Li, F. Xu, Y. Li, N. Li, H. Yu, B. Yuanb, et al., An ultrahigh 84.3% fill factor for efficient CH3NH3PbI3 P-i-N perovskite film solar cell, Sol. Energy 233 (2022) 271–277, https://doi.org/10.1016/j.solener.2022.01.035.
[57] Y. Chen, X. Xu, N. Cai, S. Qian, R. Luo, Y. Huo, et al., Rational design of dopant-free coplanar D-π-D hole-transporting materials for high-performance perovskite solar cells with fill factor exceeding 80%, Adv. Energy Mater. 9 (2019) 1901268 https://doi.org/10.1002/aenm.201901268.
[58] A.K. Das, R. Mandal, D.K. Mandal, Impact of HTM on lead-free perovskite solar cell with high efficiency, Opt. Quant. Electron. 54 (2022) 455, https://doi.org/10.1007/s11082-022-03852-z.
[59] M. Lazemi, S. Asgharizadeh, S. Bellucci, A computational approach to interface engineering of lead-free CH3NH3SnI3 highly-efficient perovskite solar cells, Phys. Chem. Chem. Phys. 20 (2018) 25683–25692, https://doi.org/10.1039/C8CP03660H.
[60] C.-C. Chueh, C.-Z. Li, A.K.Y. Jen, Recent progress and perspective in solution-processed Interfacial materials for efficient and stable polymer and organometal perovskite solar cells, Energy Environ. Sci. 8 (2015) 1160–1189, https://doi.org/10.1039/C4EE03824J.
[61] J. Xia, Y. Zhang, M. Cavazzini, S. Orlandi, B. Ding, H. Kanda, et al., Asymmetrically substituted 10H,10'H-9,9'-Spirobi[acridine] derivatives as hole-transporting materials for perovskite solar cells, Angew Chem. Int. Ed. Engl. 61 (2022) e202212891, https://doi.org/10.1002/anie.202212891.
[62] C.H. Ng, T.S. Ripolles, K. Hamada, S.H. Teo, H.N. Lim, J. Bisquert, et al., Tunable open circuit voltage by engineering inorganic cesium lead bromide/iodide perovskite solar cells, Sci. Rep. 8 (2018) 2482, https://doi.org/10.1038/s41598-018-20228-0.
[63] W. Yan, Y. Li, S. Ye, Y. Li, H. Rao, Z. Liu, et al., Increasing open circuit voltage by adjusting work function of hole-transporting materials in perovskite solar cells, Nano Res. 9 (2016) 1600–1608, https://doi.org/10.1007/s12274-016-1054-5.
[64] Y.-H. Lou, Z.-K. Wang, Aqueous-solution-processable metal oxides for high-performance organic and perovskite solar cells, Nanoscale 9 (2017) 13506–13514, https://doi.org/10.1039/C7NR04692H.
[65] W. Yan, Y. Li, Y. Li, S. Ye, Z. Liu, S. Wang, et al., High-performance hybrid perovskite solar cells with open circuit voltage dependence on hole-transporting materials, Nano Energy 16 (2015) 428–437, https://doi.org/10.1016/j.nanoen.2015.07.024.
[66] J. Stöhr, D.A. Outka, Determination of molecular orientations on surfaces from the angular dependence of near-edge x-ray-absorption fine-structure spectra, Phys. Rev. B 36 (1987) 7891–7905, https://doi.org/10.1103/PhysRevB.36.7891.
[67] A. Baby, G. Marcaud, Y.J. Dappe, M. D'Angelo, J.-L. Cantin, M.G. Silly, et al., Phthalocyanine reactivity and interaction on the 6H-SiC(0001)-(3 × 3) surface investigated by core-level experiments and simulations, Phys. Chem. Chem. Phys. 24 (2022) 14937–14946, https://doi.org/10.1039/D2CP00750A.
[68] G.-W. Kim, D.V. Shinde, T. Park, Thickness of the hole transport layer in perovskite solar cells: performance versus reproducibility, RSC Adv. 5 (2015) 99356–99360, https://doi.org/10.1039/c5ra18648j.
[69] S. Wood, D. O'Connor, C.W. Jones, J.D. Claverley, J.C. Blakesley, C. Giusca, et al., Transient photocurrent and photovoltage mapping for characterisation of defects in organic photovoltaics, Sol. Energy Mater. Sol. Cell. 161 (2017) 89–95, https://doi.org/10.1016/j.solmat.2016.11.029.
[70] T. Kirchartz, J.A. Márquez, M. Stolterfoht, T. Unold, Photoluminescence-based characterization of halide perovskites for photovoltaics, Adv. Energy Mater. 10 (2020) 1904134, https://doi.org/10.1002/aenm.201904134.